MHD NANOFLUID FREE CONVECTION FLOW OVER A VERTICALLY STRETCHING DISK WITH NONLINEAR RADIATION AND ACTIVATION ENERGY

Ephesus O. Fatunmbi
Email: ephesus.fatunmbi@federalpolyilaro.edu.ng

UNIOSUN JOURNAL OF BASIC AND APPLIED SCIENCES
OSUN STATE UNIVERSITY, OSOGBO
UJBAS

ISSN: 3121-9837
www.ujws.uniosun.edu.ng/ujbas
ujbas@uniosun.edu.ng

Authors Affiliation:

Department of Mathematics and Statistics, Federal Polytechnic, Ilaro, Nigeria

History:

Volume 1, Number 1
Published: 10/04/2026

Keywords:

Activation energy; Chemical reaction; Magneto-nanofluid; Free convective flow; Vertically stretching disk; Nonlinear thermal radiation

ABSTRACT

Free convective MHD nanofluid flow is significant due to its enhanced heat transfer characteristics coupled with wide engineering applications, including solar thermal collectors, electronic cooling systems, chemical reactors, and metallurgical operations, among others. Thus, the problem of free convective reactive magnetohydrodynamic (MHD) nanofluid transport over a vertical disk with nonlinear radiative heat flux and chemical reaction coupled with Arrhenius-type activation energy is investigated in this study. The mathematical model is expressed as a set of partial differential equations derived from the conservation laws of mass, momentum, energy, and concentration, considering the effects of Brownian motion, thermophoresis, magnetic field, and porosity on the flow field. Relevant similarity variables are employed to transform the initially developed partial differential equations into a system of nonlinear ordinary differential equations, while the required solution is numerically obtained using the Runge–Kutta–Fehlberg method together with the shooting technique. The outcomes of this computational analysis are presented graphically to illustrate the impact of the emerging physical parameters on the velocity, temperature, and concentration profiles. The results show that nonlinear thermal radiation enhances the thermal boundary layer and raises the temperature of the fluid, while increased activation energy slows down the chemical reaction rate, thereby increasing the concentration distribution of nanoparticles.

1. INTRODUCTION

The understanding of free-convective flow is essential for optimizing thermal efficiency, controlling boundary layer development, and minimizing energy losses in advanced thermo-fluid systems. The wide range of real-life applications arising from free convection in engineering and technological processes such as found in solar energy systems, nuclear reactors, cooling of electronic devices, and chemical processing equipment has attracted considerable attention from researchers (Kumar, 2001; Abro, 2020 & Jha *et al.,* 2022). Free-convective flow, otherwise known as natural convection, occurs due to the generation of buoyancy forces induced by temperature or concentration gradient within the fluid, instead of external mechanical forcing. Such phenomena are frequently encountered in natural and engineering systems where fluid motion is induced by density variations resulting from thermal heating or species diffusion. Although several geometrical configurations have been examined in the literature (Abro, 2020 & Jha *et al.,* 2022), disk-type geometries are particularly relevant to applications in rotating machinery, polymer extrusion, coating processes, and thermal material treatment, where surface heating initiates fluid motion (Khan, 2021 & Siddiqa *et al.*, 2016).

In view of its wide-ranging applications, free convective heat and mass transfer has been extensively investigated under diverse geometrical configurations and physical conditions. For instance, Krishna *et al.* (2019) analytically studied free convective micropolar fluid flow over an infinite vertical porous plate using a regular perturbation method, incorporating the effects of an inclined magnetic field, Hall current, thermal radiation, and chemical reaction. Dinarvand and Pop (2017) examined laminar free convection and thermal behavior of an electrically conducting fluid under magnetic field influence over a rotating vertical cone. Fatunmbi *et al.* (2022) numerically analyzed free convective flow over an exponentially stretching sheet, accounting for boundary slip, buoyancy forces, viscous dissipation, and radiative heat flux. The same phenomenon was further studied by Ahmed et al. (2023) on a vertically stretching disk, incorporating Brownian motion and thermophoretic effects. However, the ever-increasing requirement for better thermal efficiency in contemporary engineering and technological structures calls for the utilization of highly efficient heat transmission fluids, such as nanofluids, to optimize system performance in these fields.

Nanofluids are colloidal blend of nanoparticles suspended in base fluids (e. g. water, oil, ethylene glycol, etc.), resulting in better thermal conductivity of those fluids and improving convective heat transfer characteristics than those of ordinary fluids (Choi 1995 & Devendiran, 2016). The dispersion of nanoparticles significantly improves the thermophysical properties of base fluids, enabling diverse applications in transport and automotive engineering, pharmaceutical and drug manufacturing, solar energy systems, heat exchangers, electronic device cooling, aerospace thermal management, and biomedical drug delivery (Devendiran, 2016; Nadeem, 2016 & Mishra, 2021). Several nanofluid models have been proposed in the literature; however, the Buongiorno model distinctly identifies Brownian motion and thermophoresis as the dominant mechanisms responsible for nanoparticle transport (Nadeem, 2016; Mishra2021 & Turkyilmazoglu, 2017 & 2021). This model introduces additional terms into the energy and nanoparticle concentration equations, providing a more realistic description of coupled heat-mass transfer processes. Consequently, application abounds in predicting heat transfer enhancement in solar collectors, electronic cooling systems, and biomedical thermal applications. Accordingly, many researchers have employed this framework (Turkyilmazoglu, 2021 & Fatunmbi, 2023). For instance, Alao *et al.* (2025) examined the thermal and unsteady flow characteristics of nanofluids using the Tiwari–Das model over an expanding or contracting porous channel, Fatunmbi and Adeniyan (2020) numerically analyzed MHD micropolar nanofluid flow over a nonlinearly stretching sheet with thermal radiation and variable thermophysical properties, while Salawu *et al.* (2021) investigated heat and mass transfer in MHD Maxwell nanofluid flow over an expanding plate with nonuniform fluid properties. However, incorporating thermal radiation, and particularly the nonlinear type in the flow and heat transfer dynamics of nanofluids has been found to be crucial in various engineering applications.

Thermal radiation describes heat transfer through electromagnetic waves. In flow regimes characterized by large temperature differences, nonlinear thermal radiation provides a more accurate representation of heat transfer phenomena. Such conditions arise in diverse engineering and technological applications, including solar energy systems, astrophysical flows, advanced electronic cooling (such as electronic ship cooling), and glass and polymer manufacturing processes. In this regard, Guedri *et al.* (2023) developed an unsteady mathematical model to examine the thermal efficiency of a micropolar nanofluid over a contracting plate under nonlinear thermal radiation effects. Their results indicated an improvement in the non-dimensional Nusselt number due to the magnification of thermal radiation parameter. Makinde *et al.* (2017) investigated boundary-layer flow dynamics of a micropolar fluid over an expanding surface incorporating melting heat transfer effects. Fatunmbi and Adeniyan (2020) numerically analyzed magneto-micropolar fluid flow with nonlinear thermal radiation and entropy generation, reporting an enhancement of the thermal field with increasing temperature ratio parameter. Tong *et al.* (2021) extended this concept to a non-Newtonian Oldroyd-B nanofluid, accounting for slip effects, activation energy, convective thermal conditions, and Cattaneo–Christov heat flux.

Chemical reactions, together with activation energy, play a significant role in free convective flow mechanisms, particularly in systems where heat and mass transfer are coupled. The presence of this term alters the species concentration field and, consequently, modifies the buoyancy force arising from thermal and/or concentration gradients. These modifications directly influence the velocity, thermal, and concentration properties of the flow (Hamid, 2018 & Khan, 2020). Moreover, the least energy needed for a chemical reaction to occur in a system is termed as activation energy. It is a fundamental parameter in kinetics, which describes the relationship between temperature and reaction rates. In various scientific and engineering fields, including materials engineering, environmental systems, and thermal engineering, coupled chemical reactions with activation energy are essential in the analysis of heat transfer properties, combustion reactions, solar thermochemical systems, and pollutant degradation mechanisms (Khan, 2020; Majeed, 2018 & Fatunmbi, 2020). Thus, many researchers have considered the effects of these terms, particularly in heat-mass related systems in different geometries. For instance, Goud and Dharmaiah (2023) examined the influence of activation energy alongside Ohmic heating on nanofluid flow under linear thermal radiation, reporting an increase in concentration profiles with higher activation energy. The analysis of heat-mass transfer in a Casson nanofluid experiencing activation energy, viscous dissipation, and non-Fourier heat flux over an inclined expanding plate was considered by Meenakumari *et al.* (2025), whereas Elbashbeshy *et al.* (2023) employed the Legendre–Galerkin numerical method to study the role of activation energy in heat–mass transfer flow with Marangoni effects over a circular surface. Additional relevant studies can be found in Majeed et al. (2023); Mustafa (2017); Fatunmbi *et al.* (2023) & Salawu et al., (2024a & 2024b). However, none of these studies has reported on the flow and heat-mass transfer mechanism of the combined effects of these parameters over a disk in spite of various applications.

Thus, the present study aims to combine the effects of these parameters to investigate the flow dynamics and heat-mass transfer phenomena of nanofluid over a vertically stretching disk. The formulated model incorporates the effects of chemical reaction, porous medium, magnetic field, nonlinear thermal radiation, internal heat source, and Arrhenius activation energy on free convective heat–mass transfer in nanofluids using Buongiorno's model. The novelty of the study lies in the simultaneous incorporation of these physical mechanisms within a single mathematical framework, which allows for a more realistic description of the flow and heat–mass transfer processes. This extended model provides deeper insight into their coupled influence over the disk, thereby enhancing the predictive capability of existing models. The governing equations are solved numerically, and the results are presented graphically and discussed with relevance to real-life engineering and technological applications. The outcomes of this study provide valuable insights into improving thermal and mass transport performance in advanced energy systems, the design and optimization of modern thermo-fluid materials, chemical reactors, and other high-temperature process systems.

2. Problem Formulation and Modelling

The development and formulation of the descriptive equations for the present investigation are premised on the assumptions that the flow is non-transient, incompressible and moves over a three-dimensional radially stretchy disk consisting of minutes nanoparticles. The 3D radially stretching disk model accounts for radial expansion from the centre of the disk with a velocity proportional to radial distance. The thermophysical properties of the fluid are taken to be uniform apart from the buoyancy term included in the momentum equation. The surface coordinate system is symbolized by (x, y, z) while the disk stretches linearly in both x and y directions. The velocities at the wall are represented by $u_w = \zeta x$ and $v_w = \zeta y$ in both directions respectively. The temperature differences between the surface and the ambient fluid induces free convection effects while a uniform transverse magnetic field B_0 is applied along the z-direction without consideration for induced magnetic field. The strength of the magnetic field is defined as B_0. This uniform magnetic field simplifies this analysis while still being able to account for the essential electromagnetic effects produced by fluid flow. The thermal field is assumed to experience large difference in the temperature and as such, the nonlinear thermal radiation is applied. A uniform volumetric heat generation/absorption with rate Q_0

included in the thermal region without considering viscous dissipation effects. The nanoparticle concentration is developed using the Buongiorno model which incorporates Brownian motion and thermophoresis influence of the tiny particles. In the mass concentration field, a first-order irreversible chemical reaction is included with the Arrhenius activation energy.

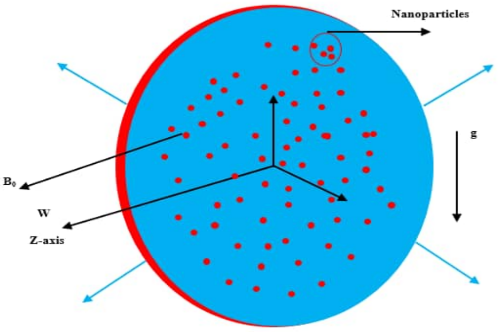

Figure 1: Flow Geometry

2.1. Governing Equations

In reference to highlighted assumptions and considering boundary layer and Boussinesq approximations, the relevant governing equations are thus stated (Ahmed *et al.,* 2023).

$$\frac{\partial u}{\partial x}+\frac{\partial v}{\partial y}+\frac{\partial w}{\partial z}=0, \tag{1}$$

$$u\frac{\partial u}{\partial x}+v\frac{\partial u}{\partial y}+w\frac{\partial u}{\partial z}=\vartheta\left(\frac{\partial^2 u}{\partial x^2}+\frac{\partial^2 u}{\partial y^2}+\frac{\partial^2 u}{\partial z^2}\right)+g_0\,(T-T_\infty)-\left(\frac{\sigma B_0^2}{\rho}\,u+\frac{\vartheta}{Kp}\,u\right), \tag{2}$$

$$u\frac{\partial v}{\partial x}+v\frac{\partial v}{\partial y}+w\frac{\partial v}{\partial z}=\vartheta\left(\frac{\partial^2 v}{\partial x^2}+\frac{\partial^2 v}{\partial y^2}+\frac{\partial^2 v}{\partial z^2}\right)-\left(\frac{\sigma B_0^2}{\rho}\,v+\frac{\vartheta}{Kp}\,v\right), \tag{3}$$

$$u\,\frac{\partial w}{\partial x}+v\,\frac{\partial w}{\partial y}+w\,\frac{\partial w}{\partial z}=-\frac{1}{\rho}\frac{\partial p}{\partial z}+\vartheta\left(\frac{\partial^2 w}{\partial x^2}+\frac{\partial^2 w}{\partial y^2}+\frac{\partial^2 w}{\partial z^2}\right), \tag{4}$$

$$\begin{gathered}u\,\frac{\partial T}{\partial x}+v\,\frac{\partial T}{\partial y}+w\,\frac{\partial T}{\partial z}=\frac{k}{\rho c_p}\left(\frac{\partial^2 T}{\partial x^2}+\frac{\partial^2 T}{\partial y^2}+\frac{\partial^2 T}{\partial z^2}\right)+\frac{16\sigma^*}{3k^*\rho c_p}\frac{\partial}{\partial z}\left(T^3\frac{\partial T}{\partial z}\right)+\frac{Q_0(T-T_\infty)}{\rho c_p}\\ \tau_1\left[D_B\left(\frac{\partial N}{\partial x}\frac{\partial T}{\partial x}+\frac{\partial N}{\partial y}\frac{\partial T}{\partial y}+\frac{\partial N}{\partial z}\frac{\partial T}{\partial z}\right)+\frac{D_t}{T_\infty}\left\{\left(\frac{\partial T}{\partial x}\right)^2+\left(\frac{\partial T}{\partial y}\right)^2+\left(\frac{\partial T}{\partial z}\right)^2\right\}\right],\end{gathered} \tag{5}$$

$$u\frac{\partial N}{\partial x}+v\frac{\partial N}{\partial y}+w\frac{\partial N}{\partial z}=D_B\left(\frac{\partial^2 N}{\partial x^2}+\frac{\partial^2 N}{\partial y^2}+\frac{\partial^2 N}{\partial z^2}\right)+\frac{D_t}{T_\infty}\left\{\frac{\partial^2 T}{\partial x^2}+\frac{\partial^2 T}{\partial y^2}+\frac{\partial^2 T}{\partial z^2}\right\}- \\ k_0(N-N_\infty)\left(\frac{T}{T_\infty}\right)^n\exp\left(-\frac{E_a}{R_gT}\right). \tag{6}$$

The respective conditions at the wall for the controlling equations (1) --(6) are expressed as:

$$\begin{aligned} &u(x,y,0)=u_w(x), v(x,y,0)=v_w(y), w(x,y,0)=0, \\ &T(x,y,0)=T_w, N(x,y,0)=N_w, z=0; \\ &u\to 0, v\to 0, T\to T_\infty, N\to N_\infty, P\to P_\infty, z\to\infty. \end{aligned} \tag{7}$$

In these equations, the respective components of velocities are $u_w(x)$ and $v_w(y)$ along the x and y directions. The conditions at the stretching surface ($z=0$) assumes that the fluid adheres to the surface and transport with those velocities in the x- and y-directions, and such, no-slip condition is assumed. At the same time, there is no fluid penetration through the surface, The surface temperature and concentration are taken to be constant $T=T_w$ and $N=N_w$. The conditions at far field from the surface ($z\to\infty$) signifies that the stretching influence vanishes, and the fluid is quiescent in the free stream. More so, the temperature approaches the ambient value T_∞ while the nanoparticle concentration approaches the ambient value N_∞, indicating mass transfer equilibrium. The pressure approaches the free-stream pressure far from the surface ($P\to P_\infty$).

2.2. Similarity transformation

$$\eta=z\left(\frac{\zeta}{\vartheta}\right)^{1/2}, u=\left(\frac{\beta g_0(T_w-T_\infty)}{\zeta}\right)h(\eta)+\zeta xf'(\eta), v=\zeta yf'(\eta), w=-2(\zeta\vartheta)^{1/2}f(\eta), \\ \theta(\eta)=\frac{T-T_\infty}{T_w-T_\infty}, \phi(\eta)=\frac{N-N_\infty}{N_w-N_\infty} \tag{8}$$

Upon substituting quantities (8) into equations (1-6) together with the wall conditions (7), the underlisted ODEs are obtained:

$$f'''(\eta)+2f(\eta)f''(\eta)-(f'(\eta))^2-(M+\beta_0)f'(\eta)=0, \tag{9}$$

$$f'(\eta)G(\eta)-2f(\eta)G'(\eta)-G''(\eta)+(M+\beta_0)G(\eta)-\Lambda\theta(\eta)=0, \tag{10}$$

$$[1+Nr(b-1)\theta+1)^3]\theta''(\eta)+3((b-1)\theta(\eta))^2(b-1)\theta'^2+2Prf(\eta)\theta'(\eta)+ \\ PrQ\theta(\eta)+PrNt(\theta')^2(\eta)+PrNb\theta'(\eta)\phi'(\eta)=0 \tag{11}$$

$$\phi''(\eta)+2Scf\phi'(\eta)+\frac{Nt}{Nb}\theta''(\eta)-Kr[(b-1)\theta(\eta)+1]^n\exp\left(\frac{E}{(b-1)\theta(\eta)+1}\right)\phi(\eta)=0 \tag{12}$$

From the z-component of the momentum equation (4), the normalized pressure term is obtained thus:

$$p'(\eta) = -\rho\,\zeta\,\vartheta\,(2\,f''(\eta) + 4\,f(\eta)f'(\eta)), \tag{13}$$

$$p(\eta) = -2\,\rho\,\zeta\,\vartheta\,(f'(\eta) + f(\eta)^2) + C, \tag{14}$$

$$P(\eta) = \frac{p(\infty) - p(\eta)}{2\rho\vartheta\zeta} = f(\eta)^2 + f'(\eta) - f(\infty)^2. \tag{15}$$

Moreover, equation (16) shows the transmuted wall conditions as:

$$\begin{gathered} f(\eta) = 0, f'(\eta) = 1, G(\eta) = 0, \theta(\eta) = 1, \phi(\eta) = 1, \text{at } \eta = 0 \\ f(\infty) = 0, G(\infty) = 0, \theta(\infty) = 0, \phi(\infty) = 0. \end{gathered} \tag{16}$$

Equation (18) is the emerging physical quantities derivable from the descriptive equations. Their descriptions are recorded in Table 1:

$$\begin{gathered} M = \frac{\sigma B_0^2}{\zeta \rho_f}, \beta_0 = \frac{\vartheta}{\zeta Kp}, \Lambda = \frac{g_0 \beta (Tw - T_\infty)}{\zeta H}, Nr = \frac{16\sigma^* T_\infty^3}{k^* k_f}, Pr = \frac{(\mu c_p)}{k}, b = \frac{T_w}{T_\infty}, \\ Sc = \frac{\vartheta}{D_B}, Nt = \frac{\gamma D_t (T_w - T_\infty)}{\vartheta T_\infty}, Nb = \frac{\gamma D_B (N_w - N_\infty)}{\vartheta}, Kr = \frac{k_0}{\zeta}, \gamma = \frac{E_a}{R_g T_\infty} \\ where\ H = \left(\frac{\beta g_0 (T_w - T_\infty)}{\zeta}\right) h(\eta). \end{gathered} \tag{17}$$

The various symbols and letters used for representing various quantities and parameters as featured in equations (1-21) are described in Table 1.

Table 1: Symbolic description of various letters and parameters

Symbols	**Symbols description**	**Symbols**	**Symbols description**
u, v, w	velocity components	T	temperature
ϑ	kinematic viscosity	n	fitted rate constant
ρ	fluid density	T_w	surface temperature
μ	fluid viscosity	Pr	Prandtl number
k	fluid thermal conductivity	b	nonlinear thermal radiation parameter
σ	electrical conductivity	T_∞	free stream temperature
N_∞	concentration at upstream	Λ	Convective parameter
Nt	thermophoresis parameter	Q_0	Coefficient of heat generation
k_o	Chemical rate of reaction	Sc	Schmidt number
N_w	concentration at upper disk	N	concentration

Nb	Brownian term	E_a	Activation energy parameter
Kp	permeability of the porous medium	β_0	porosity parameter
P	Pressure	Nr	thermal radiation parameter
(ρc_p)	heat capacity	g_0	gravitational acceleration
k	thermal conductivity	R_g	Boltzmann constant
E	activation energy parameter	Kr	chemical reaction parameter

2.3. Quantities of Engineering Interest

The skin frictional factor, local Nusselt and Sherwood numbers are included as the physical quantities of interest, they are respectively described as follows:

$$\begin{cases} C_{fx} = \dfrac{\tau_{wx}}{\rho(\zeta x)^2} \\ Nu_x = \dfrac{x q_w}{k\,(T_w - T_\infty)} \\ Sh_x = \dfrac{x j_w}{D_B(N_w - N_\infty)}. \end{cases} \tag{18}$$

Where

$$\begin{cases} \tau_{wx} = \mu\left(\dfrac{\partial u}{\partial z}\right)_{z=0} \\ q_w = -k\left(\dfrac{\partial T}{\partial z}\right)_{z=0} \\ j_w = -D_B\left(\dfrac{\partial N}{\partial z}\right)_{z=0}. \end{cases} \tag{19}$$

The respective quantity in equation (19) is simply the wall shear stress heat flux and mass flux. Using the similarity transformation variables (9) to obtain the complete non-dimensional physical quantities expression:

$$\begin{cases} C_{fx}Re_x^{1/2} = f''(0) + \Lambda h'(0) \\ Nu_x Re_x^{-1/2} = -\theta'(0) \\ Sh_x Re_x^{-1/2} = -\phi'(0). \end{cases} \tag{20}$$

Where the local Reynolds number is denoted by:

$$Re_x = \frac{\zeta x^2}{\vartheta}, \tag{21}$$

3.0 Solution Methodology

The solution to the transformed equations (12--16) is obtained numerically by employing the shooting technique together with Runge-Kutta-Fehlberg method (RKFM). This technique is used due to the high nonlinearity of the governing equations, which makes obtaining closed-form analytical solutions practically impossible. The shooting method is engaged to convert the BVP into an IVP by guessing the unknown initial conditions, integrating the system, and iteratively adjusting the guesses until the boundary conditions at infinity are satisfactorily obtained. The RKFM is then used to integrate the resultant set of first-order ordinary derivatives. The RKFM provides highly accurate, stable, and efficient results for nonlinear differential equations. It automatically adjusts the step size to maintain the desired error tolerance, making it particularly suitable for stiff or sensitive systems. Various authors have used RKFM and shooting methods in the literature due to its reliability and accurate numerical solutions. The numerical computation was done using an initial step size of 0.01 with a convergence criterion of 10^{-6}, while the upstream boundary condition at infinity was truncated at $\eta_\infty = 8$. With the introduction of nine state variables:

$$\begin{cases} y_1(\eta) = f(\eta), y_2(\eta) = f'(\eta), y_3(\eta) = f''(\eta), \\ y_4(\eta) = G(\eta), y_5(\eta) := G'(\eta), \\ y_6(\eta) = \theta(\eta), y_7(\eta) := \theta'(\eta), \\ y_8(\eta) = \phi(\eta), y_9(\eta) = \phi'(\eta). \end{cases} \tag{22}$$

Using the definitions above, the equivalent first-order system $y_i' = F_i(\eta, y_1, \dots, y_9)$ is

$$\begin{cases} y_1' = y_2, y_2' = y_3, \\ y_3' = -2\, y_1\, y_3 + y_2^2 + (M + \beta_0)\, y_2, \\ y_4' = y_5, \\ y_5' = y_2\, y_4 - 2\, y_1\, y_5 + (M + \beta_0)\, y_4 - \Lambda\, y_6, \end{cases} \tag{23}$$

For the energy equation, we define the auxiliary coefficient

$$B(y_6) := 1 + Nr((b-1)y_6 + 1)^3.$$

Then the equation for $y_7' = \theta''$ becomes

$$y_7' = -\frac{3((b-1)y_6 + 1)^2(b-1)\, y_7^2 + 2Pr\, y_1\, y_7 + Pr\, Q\, y_6 + Pr\, Nt\, y_7^2 + Pr\, Nb\, y_7\, y_9}{B(y_6)} \tag{24}$$

Consequently, the concentration equation gives $y_9' = \phi''$. Upon substitution into the governing equation, we obtain

$$y_8' = y_9,$$
$$y_9' = -2Sc\, y_1\, y_9 - \frac{Nt}{Nb} y_7' + Kr((b-1)y_6+1)^n \exp\left(\frac{\gamma}{(b-1)y_6+1}\right) y_8, \qquad (25)$$

For the boundary conditions, the transformed conditions both at the wall ($\eta = 0$) and at far field $\eta \to \infty$ are:

At $\eta = 0$ (wall)and at the far field $\eta \to \infty$ are respectively given as:

$$\begin{cases} y_1(0) = 0, y_2(0) = 1, y_4(0) = 0, y_6(0) = 1, y_8(0) = 1 \\ y_1(\infty) = 0, y_4(\infty) = 0, y_6(\infty) = 0, y_8(\infty) = 0 \end{cases} \qquad (26)$$

There are four initial derivatives that are unspecified at $\eta = 0$, these are

$y_3(0) = f''(0) =: s_1, y_5(0) = G'(0) =: s_2, y_7(0) = \theta'(0) =: s_3, y_9(0) = \phi'(0) =: s_4.$

Thus, the IVP initial vector at $\eta = 0$ is

$\mathbf{Y}(0) = [\, 0, 1, s_1, 0, s_2, 1, s_3, 1, s_4 \,]^{\mathsf{T}}.$

Table 2 shows the computed values of the temperature gradient $-\theta'(0)$ and the microrotation gradient $G'(0)$ for different Prandtl numbers, as compared with previously published results (Ahmed *et al.,* 2023; Wang, 2007). As demonstrated in the table, an excellent agreement is observed from the present findings as compared with previous data under some limiting scenarios, thereby validating the accuracy and reliability of the current numerical scheme.

Table 2: Data of temperature gradient $-\theta'(0)$ and skin friction coefficient $G'(0)$ for varying Pr as compared with published works when $R = M = Nt = E = Sc = \delta = n = 0, Nb = 0.0001, b = 1, Gr = 1$.

Pr	**Wang (2007)**		**Ahmed *et al.* (2023)**		**Present study**	
	$-\theta'(0)$	$G'(0)$	$-\theta'(0)$	$G'(0)$	$-\theta'(0)$	$G'(0)$
0.2	0.25165	1.77962	0.254524	1.700592	0.250738	1.710367
0.7	0.66726	0.70658	0.666584	0.706789	0.667811	0.703440
2.0	1.32391	0.38407	1.323333	0.383630	1.323898	0.384067
7.0	2.72297	0.20331	2.726175	0.203049	2.722963	0.203307
20	4.78914	0.12164	4.840868	0.124378	4.789126	0.121645

70	9.18731	0.06593	8.430984	0.068906	9.187282	0.065928
200	15.7061	0.03933	15.966011	0.03701	15.706043	0.039329

4. Results Analysis and Discussion

Here, many graphs are presented to showcase the impact of some physical parameters on the non-dimensional transport profiles. Unless otherwise stated in the figures, the default computational parameter values employed for various graphs as carefully selected from existing related studies are: $Nr = 0.5, Kr = 0.3, Pr = 7, Gr = 0.5, Nt = 0.7, Sc = 0.62, b = 2.5, \beta_0 = M = Nb = E_a = 0.5, n = 1.0, m = 0.2, Q = 0.1$

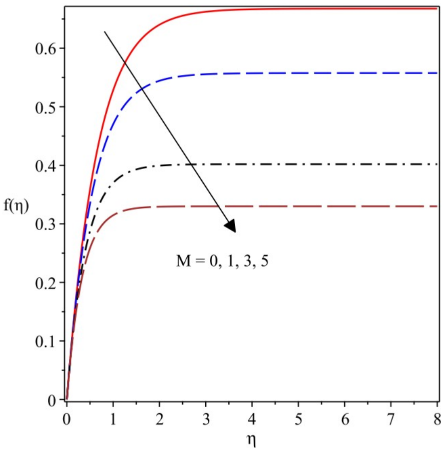

Figure 2: Axial velocity plot for varying M

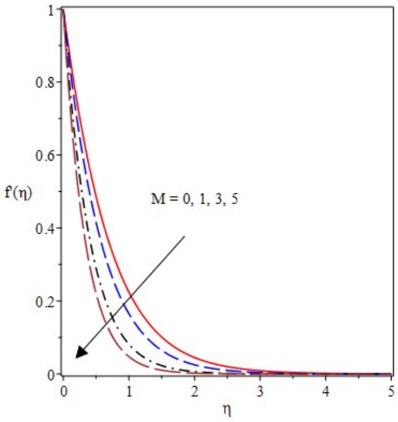

Figure 3: Radial Velocity plot for M

In Figure 2, the character of M on the axial velocity curves is presented. There is a consistent decline of this profile as the magnetic parameter increases. This behaviour arises because a higher M induces a stronger Lorentz force that opposes the axial motion of the conducting fluid, weakens momentum transport, and reduces the boundary layer thickness. Hence, larger magnetic field strengths suppress axial fluid spreading over the disk. Similarly, the radial velocity profile diminishes with increasing M as pictured in Figure3. This trend indicates that the Lorentz force counteracts the buoyancy-driven upward motion, thereby reducing the intensity of natural convection. Consequently, an increase in M produces a thinner boundary layer and suppresses the radial velocity.

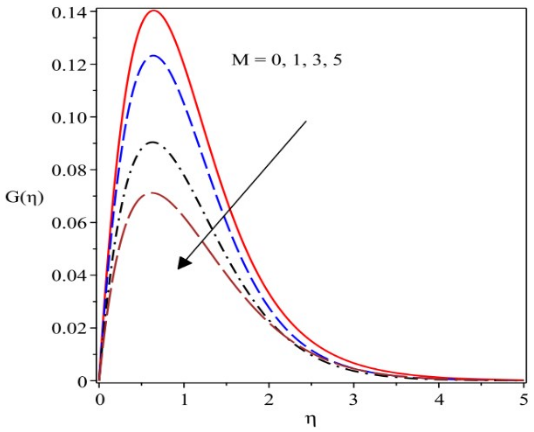

Figure 4:Tangential velocity curve for varying M

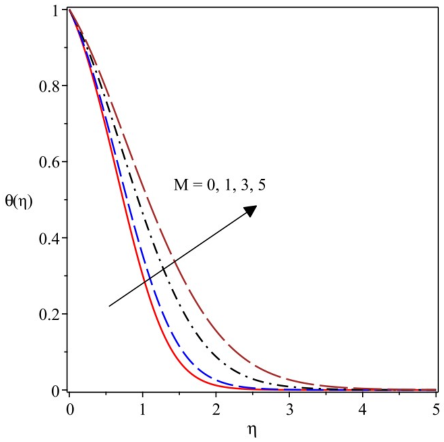

Figure 5: Thermal profile for changes in M

Figure 4 illustrates the tangential velocity profile (f^' (η)) as M increases. From the graph, observation reveals that the applied magnetic field suppresses the swirl motion of the electrically conducting fluid. As G(η) tends to zero, the profile is consistent with the far- boundary condition, indicating that stronger magnetic fields effectively reduce the strength of rotational motion in the flow. Contrary to trend in Figure 4, the temperature profile magnifies with increasing M as demonstrated in Figure 5. Such occurrence stemmed from the impact of the Lorentz force which acts as a resistive drag, reducing the fluid velocity and thereby decreasing convective heat transfer further from the disk, which thickens the thermal boundary layer. The electrically conducting nanofluid induces Ohmic heating, which correspondingly boost the energy in the fluid. Consequently, an increase in M elevates the fluid temperature, suggesting that magnetic effects can be utilized to control thermal retention in magneto-nanofluid flow applications.

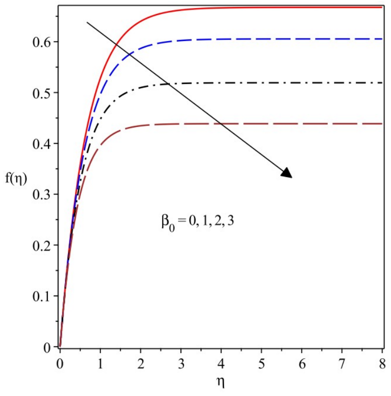

Figure 6: Axial velocity curve for varying β_0

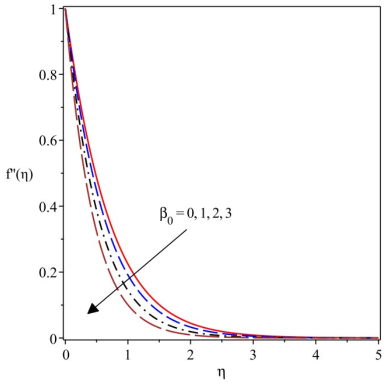

Figure 7: Radial velocity profile for β

Figures 6, 7, and 8 show that the axial, radial, and tangential velocity profiles decrease as the porous parameter β_0 increases. This reduction is due to the resistive Darcy drag of the porous medium, which opposes fluid motion and thickens the momentum boundary layer. In contrast, Figure 9 illustrates growth in the temperature profile emanating from escalating values of β_0. The slow fluid motion reduces convective heat removal from the disk, while viscous and Ohmic dissipation within the porous medium add energy to the fluid. Consequently, higher β_0 values enhance thermal retention in the magneto-nanofluid flow.

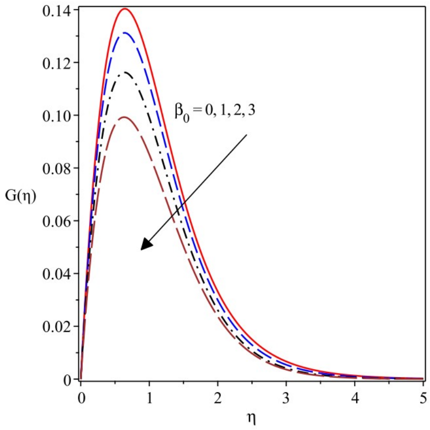

Figure 8: Tangential velocity curve for β_0

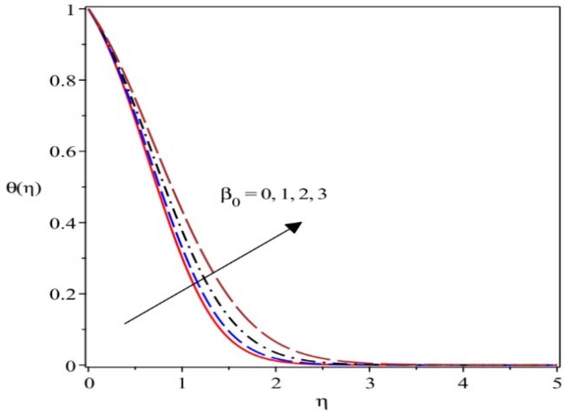

Figure 9: Thermal variation for rising β_0

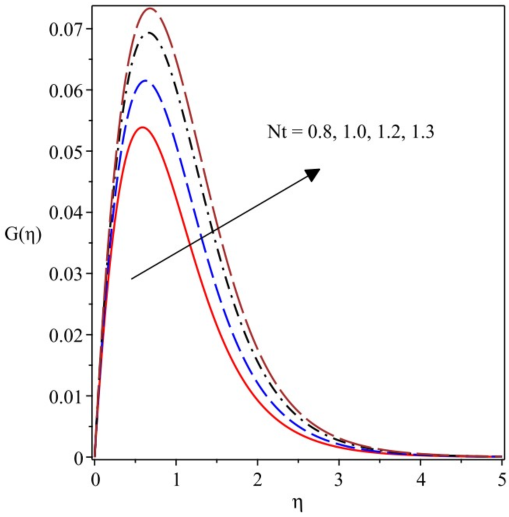

Figure 10: Tangential velocity for varying Nt

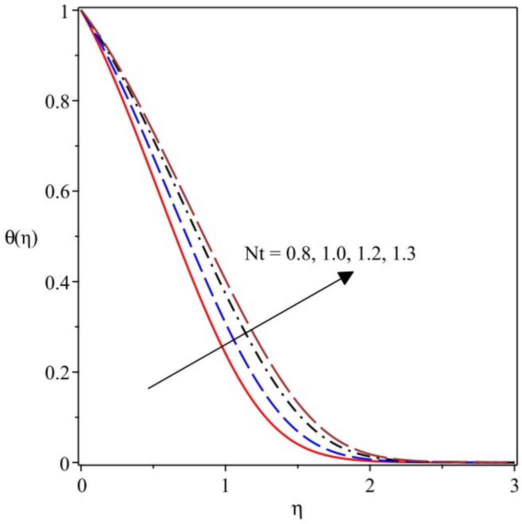

Figure 11: Thermal profiles for Nt

Figures 10, 11, and 12 show the impacts of Nt on the profile of the tangential velocity, thermal and concentration distribution, respectively. Observation reveals that there a lift in all the three profiles as Nt upsurges. In the physical sense, the term thermophoresis induces a migration of the nanoparticles from high temperature regions to lower temperature. This phenomenon improves the fluid momentum due to the extra particle flux, which slightly accelerates the tangential velocity.

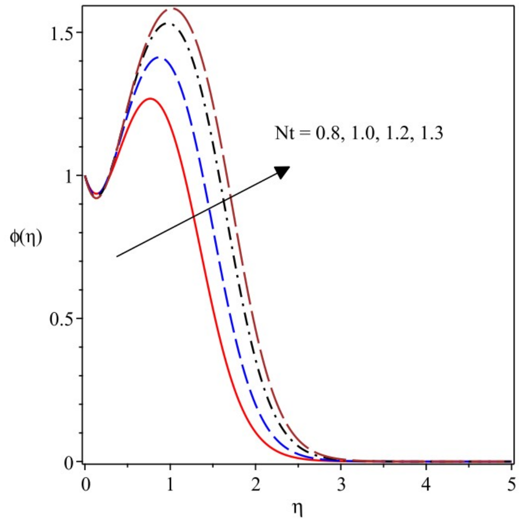

Figure 12: Concentration profile for Nt

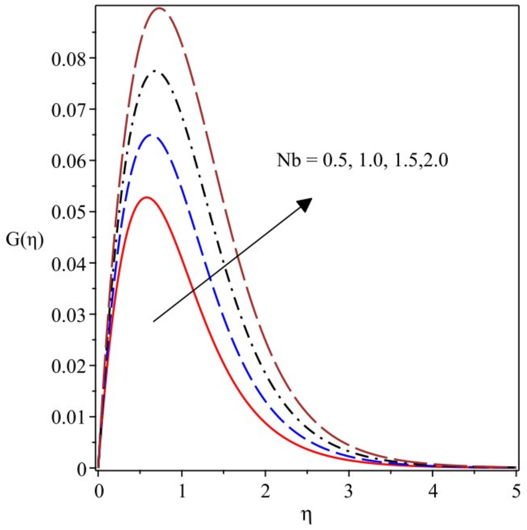

Figure 13: Tangential velocity for rising Nb

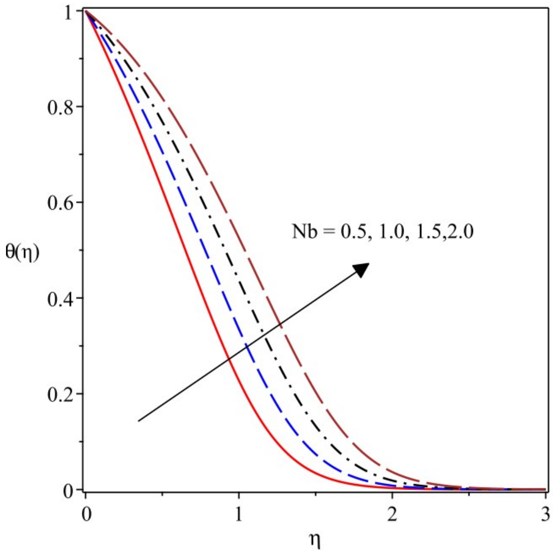

Figure 14: Thermal profile for varying Nb

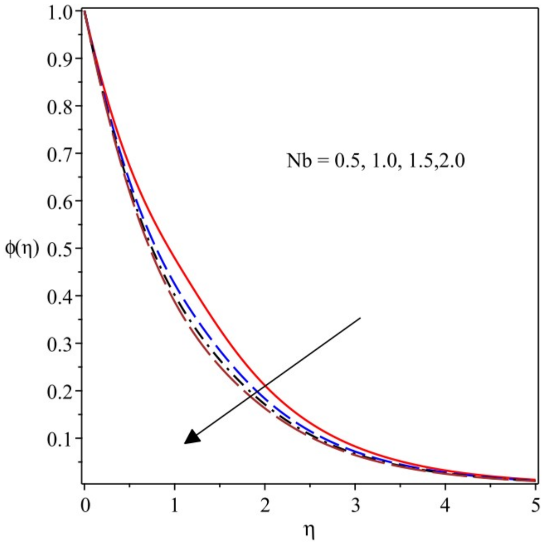

Figure 15: Concentration profile for in Nb

Also, this migration causes an accumulation nanoparticle near the surface and thereby raises the thermal energy within the boundary layer, which thus strengthens the heat distribution as depicted in Figure 11. Likewise, the nanoparticle concentration near the disk enhances due to the thermophoretic motion, thickening the concentration boundary layer. It is therefore confirmed that higher intensity of favours fluid transport mechanism as well as heat-mass transfer in the MHD nanofluid flow over a disk. As pictured in Figures 13–14, increasing the Brownian motion term (N_b) enhances the tangential transport mechanism and significantly elevates the heat distribution in the system. This behaviour occurs because a higher (N_b) intensifies the random motion of nanoparticles, thereby increasing microscopic energy exchange and promoting thermal energy transport in the fluid. Consequently, the heat bounding surface layer increases. In contrast, the concentration profile decreases with increasing (N_b), as shown in Figure 15. This reduction is attributed to the intensified random movement of nanoparticles, which promotes their diffusion away from the disk surface, thereby weakening nanoparticle accumulation near the wall and reducing concentration levels within the boundary layer.

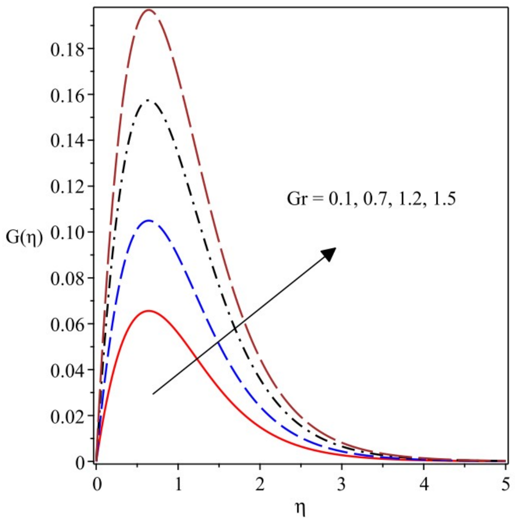

Figure 16: Velocity profiles for varying Gr

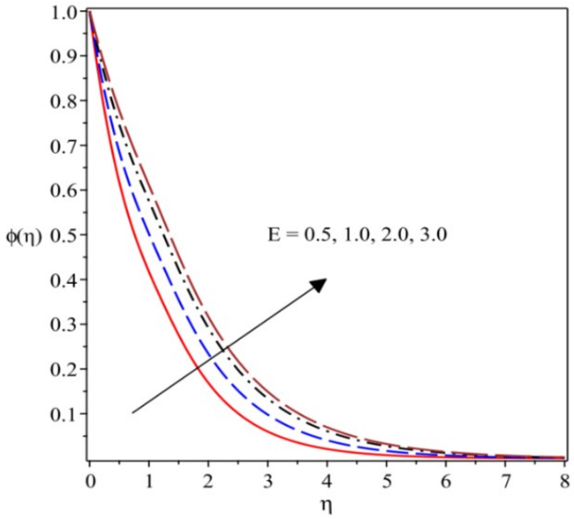

Figure 17: Concentration profiles for E

It is observed in Figure 16 that the tangential velocity accelerates due to rising values of Gr. This is because the buoyant force in the flow field increases as Gr magnifies. This buoyant force overcomes the viscous resistance in the flow field, thereby increasing the velocity. The impact of activation energy   on the profile is depicted in Figure 17. From the figure, it is noted that with the increase in E, the rate at which a chemical reaction occurs in the fluid is reduced. This is because, with high activation energy, a significant amount of energy is required for a reaction to take place, thus a reduced rate, and hence the consumption of the species is reduced. This leads to an increase in the nanoparticle concentration profile $\phi(\eta)$.

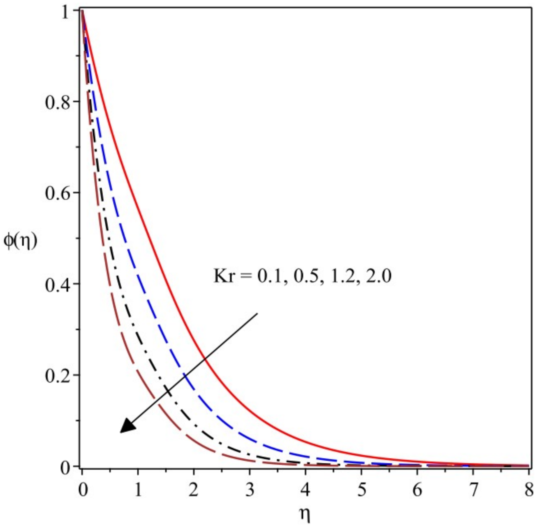

Figure 18: Concentration profile for Kr

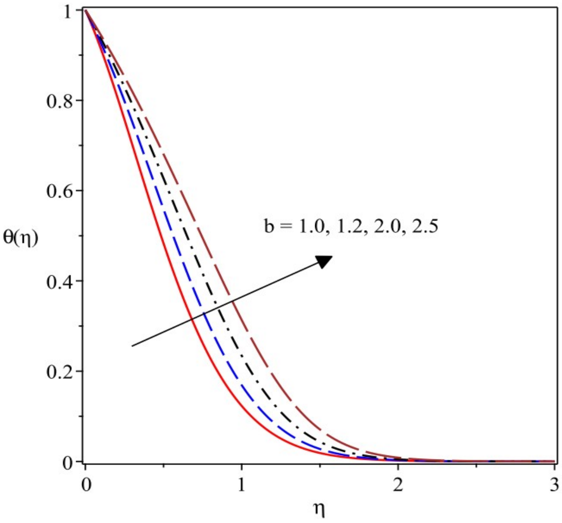

Figure 19: Temperature profile for rising b

Figure 18 captures the reaction of the nanoparticle concentration profile $(\phi(\eta))$ as Kr varies in magnitude. From this graph, there is a decline in the concentration profile as the magnitude of Kr increases. This is because when Kr increases, it promotes the rate of the chemical reaction, which boost the rate at which nanoparticles are consumed near the surface of the disk, hence reducing the concentration profile. As shown in Figure 19, the impact of the nonlinear radiation parameter b on the temperature distribution is presented. It can be noted that the temperature profile increases with an increase in the value of b. This happens because the nonlinear form of thermal radiation increases the radiative heat flux in the fluid. Consequently, additional thermal energy is transferred to the fluid, leading to an increase in the thermal boundary layer and the temperature profile.

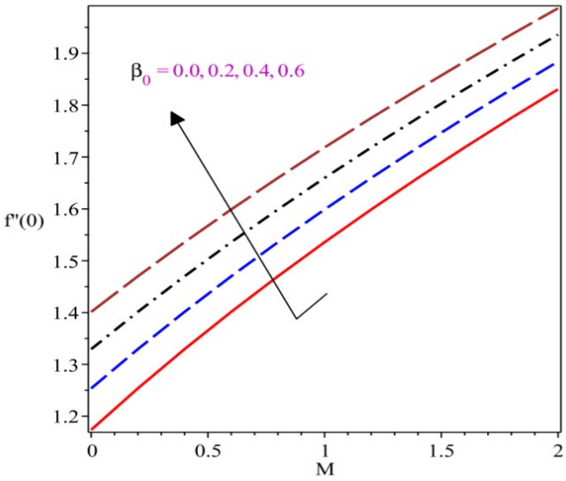

Figure 20 Radial surface drag for varying β_0

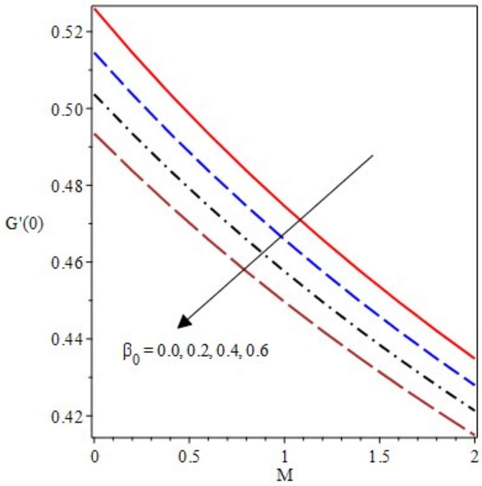

Figure 21: Tangential surface drag for β_0

The drag on the radial surface $(f''(0))$ is seen to increase with an increase in the porosity parameter β_0, as depicted in Figure 20. This is mainly because, with an increase in β_0, the resistance in the porous medium is also increased, thus slowing down the flow and increasing the shear stress on the radial surface. On the other hand, the drag on the tangential surface $(G'(0))$ is seen to decrease with an increase in β_0, as depicted in Figure 21. This occurs because the tangential momentum in the fluid is damped by the porous matrix, thus reducing the shear stress on the tangential surface.

5.0 Concluding Remarks

The phenomenon of flow and heat transfer characteristics of free convective and reactive magneto-nanofluid flow over an expanding vertical disk is analyzed in this study. The governing equations representing the physical model are formulated as coupled nonlinear partial derivatives and subsequently transformed into a system of nonlinear ordinary derivatives sing appropriate similarity transformations. The transmuted model is numerically integrated via the shooting technique combined with the Runge–Kutta–Fehlberg integration scheme. The numerical outcomes exhibited excellent agreement with previously published results under limiting conditions, thereby confirming the correctness of the present computational technique. The major findings derived from this investigation are summarized as follows:

- Magnetic parameter suppresses axial, radial, and tangential velocities due to Lorentz force effects, reducing momentum boundary layer thickness, whereas the thermal region escalates in the presence of this parameter.
- Porous parameter decreases all velocity components via Darcy resistance but increases surface drag in the tangential direction, and also temperature due to internal dissipation.
- Thermophoresis parameter enhances temperature, and nanoparticle concentration by driving particles toward cooler regions, thickening thermal and concentration boundary layers but the Brownian motion term suppresses concentration owing to nanoparticle dispersion away from the disk surface.
- The convective parameter increases tangential velocity by strengthening buoyancy forces whereas the skin frictional factor in the radial direction declines as the porosity term amplifies.
- The concentration field diminishes with higher values of the chemical reaction due to enhanced particle consumption; in the same way the activation energy increases nanoparticle concentration by slowing the chemical reaction rate. The thickness of the temperature profiles is raised as temperature ratio (nonlinear thermal radiation term) and Brownian motion

parameters elevate in the energy region.

References

Abro, K. A. (2020). Fractional characterization of fluid and synergistic effects of free convective flow in circular pipe through Hankel transform. *Physics of Fluids, 32*(12). https://doi.org/10.1063/5.0034012

Ahmed, A., Usman, M., Lu, D., Zhang, Z., Hussien, M. A., & Hassan, A. M. (2023). Numerical simulation of free convective flow over vertical disk via spectral-collocation method. *Case Studies in Thermal Engineering, 52*, 103668.

Alao, S., Salawu, S. O., Oderinu, R. A., Akinola, E. I., Oyewumi, A. A., Yahaya, A. A., & Salaudeen, K. A. (2025). Numerical computation of thermal radiation and mixed convective effect on electro-magnetized Tiwari–Das nanofluid model in a porous microchannel. *International Journal of Applied and Computational Mathematics, 11*(3), 113. https://doi.org/10.1007/s40819-025-01314-8

Choi, S. U. S. (1995). Enhancing thermal conductivity of fluids with nanoparticles. In *ASME International Mechanical Engineering Congress and Exposition*, 174. 99–105. New York, NY: American Society of Mechanical Engineers.

Devendiran, D. K., & Amirtham, V. A. (2016). A review on preparation, characterization, properties and applications of nanofluids. *Renewable and Sustainable Energy Reviews, 60*, 21–40. https://doi.org/10.1016/j.rser.2016.01.115

Dinarvand, S., & Pop, I. (2017). Free-convective flow of copper/water nanofluid about a rotating down-pointing cone using Tiwari–Das nanofluid scheme. *Advanced Powder Technology, 28*(3), 900–909.

Elbashbeshy, E. M., Fathy, M., & Abdelgaber, K. M. (2023). Effects of chemical reaction and activation energy on Marangoni flow, heat and mass transfer over circular porous surface. *Arab Journal of Basic and Applied Sciences, 30*(1), 46–54.

Nonlinear thermal radiation and entropy generation on steady flow of magneto-micropolar fluid passing a stretchable sheet with variable properties. *Results in Engineering, 6*, 100142.

Fatunmbi, E. O., & Adeniyan, A. (2020). Nonlinear thermal radiation and entropy generation on steady flow of magneto-micropolar fluid passing a stretchable sheet with variable properties. *Results in Engineering, 6*, 100142.

Fatunmbi, E. O., Mabood, F., Elmonser, H., & Tlili, I. (2020). Magnetohydrodynamic nonlinear mixed convection flow of reactive tangent hyperbolic nanofluid passing a nonlinear stretchable surface. *Physica Scripta, 96*(1), 015204.

Fatunmbi, E. O., Oke, A. S., & Salawu, S. O. (2023). Magnetohydrodynamic micropolar nanofluid flow over a vertically elongating sheet containing gyrotactic microorganisms with temperature-dependent viscosity. *Results in Materials, 19*, 100453. https://doi.org/10.1016/j.rinmat.2023.100453

Fatunmbi, E. O., Salawu, S. O., & Adeniyan, A. (2022). Buoyancy force and slip conditions on hydromagnetic dissipative flow of micropolar fluid passing an exponentially stretching sheet. *Computational Thermal Sciences, 14*(1), 45–60.

Goud, B. S., & Dharmaiah, G. (2023). Role of Joule heating and activation energy on MHD heat and mass transfer flow in the presence of thermal radiation. *Numerical Heat Transfer, Part B: Fundamentals, 84*(5), 620–641.

Guedri, K., Mahmood, Z., Fadhl, B. M., Makhdoum, B. M., Eldin, S. M., & Khan, U. (2023). Mathematical analysis of nonlinear thermal radiation and nanoparticle aggregation on unsteady MHD flow of micropolar nanofluid over shrinking sheet. *Heliyon, 9*(3), 1-13.

Hamid, A., & Khan, M. (2018). Impacts of binary chemical reaction with activation energy on unsteady flow of magneto-Williamson nanofluid. *Journal of Molecular Liquids, 262*, 435–442. https://doi.org/10.1016/j.molliq.2018.04.095

Jha, B. K., Altine, M. M., & Hussaini, A. M. (2022). Role of suction/injection on free convective flow in a vertical channel in the presence of point/line heat source/sink

Journal of Heat Transfer, 144(6), 062602. https://doi.org/10.1115/1.4053984

Khan, M. I. (2021). Transportation of hybrid nanoparticles in forced convective Darcy–Forchheimer flow by a rotating disk. *International Communications in Heat and Mass Transfer, 122*, 105177. https://doi.org/10.1016/j.icheatmasstransfer.2020.105177

Kumar, D., Singh, A. K., & Kumar, D. (2018). Effect of Hall current on magnetohydrodynamic free convective flow between vertical walls with induced magnetic field. *The European Physical Journal Plus, 133*(5), 207.

Mishra, A., & Kumar, M. (2021). Numerical analysis of MHD nanofluid flow over a wedge including viscous dissipation and heat generation/absorption using the Buongiorno model. *Heat Transfer, 50*(8), 8453–8474.

Mustafa, M., Khan, J. A., Hayat, T., & Alsaedi, A. (2017). Buoyancy effects on the MHD nanofluid flow past a vertical surface with chemical reaction and activation energy. *International Journal of Heat and Mass Transfer, 108*, 1340–1346.

Nadeem, S., Khan, A. U., & Saleem, S. (2016). A comparative analysis of different nanofluid models for oscillatory stagnation point flow. *The European Physical Journal Plus, 131*(8), 261. https://doi.org/10.1140/epjp/i2016-16261-4

Salawu, S. O., Fatunmbi, E. O., & Okoya, S. S. (2021). MHD heat and mass transport of Maxwell Arrhenius kinetic nanofluid flow over stretching surface with nonlinear variable properties. *Results in Chemistry, 3*, 100125.

Siddiqa, S., Hossain, M. A., & Gorla, R. S. (2016). Temperature-dependent density effect on natural convection flow over a horizontal circular disk. *Journal of Thermophysics and Heat Transfer, 30*(4), 890–896.

Tong, Z. W., Khan, S. U., Vaidya, H., Rajashekhar, R., Sun, T. C., Khan, M. I., Prasad, K. V., Chinram, R., & Aly, A. A. (2021). Nonlinear thermal radiation and activation energy significances in slip flow of bioconvection of Oldroyd-B nanofluid with Cattaneo–Christov theories. *Case Studies in Thermal Engineering, 26*, 101069.

Turkyilmazoglu, M. (2017). Condensation of laminar film over curved vertical walls using single and two-phase nanofluid models. *European Journal of Mechanics – B/Fluids, 65*, 184–191.

Turkyilmazoglu, M. (2021). On the transparent effects of Buongiorno nanofluid model on heat and mass transfer. The European Physical Journal Plus, 136(4), 1–5.

Wang, C. Y. (2007). Natural convection on a vertical radially stretching sheet. Journal of Mathematical Analysis and Applications, 332(2), 877–883.